Control System Performance and Efficiency for a Mid–Depth Lagrangian Profiling Float

Bryan McGilvray, Chris Roman
University of Rhode Island
Graduate School of Oceanography
Narragansett, RI, USA
brycmcg@mail.uri.edu
cnr@gso.uri.edu

***Abstract*—This paper presents the development of a new mid–depth Lagrangian profiling float with a primary emphasis on the control system performance and efficiency. While deep water floats have demonstrated much success in open ocean environments, many are not suited for the additional challenges associated with coastal regions. To study these regions, which are often subject to varying bathymetry within the operating range and higher variations in water density, a more advanced system is required. This new design utilizes pressure and altitude feedback to drive a high volume auto-ballasting system (ABS). The main operating modes of this float include step inputs to park and drift at constant depths, profiling inputs with adjustable rates and adaptable limits, and constant altitude bottom tracking. To handle these tasks, a state–space feedback control system, which uses feedback linearization to account for the nonlinear drag force acting on the moving float, was designed and simulated. Additionally, the development of the control system was coupled with empirical motor efficiency data to study the tradeoffs between efficiency and performance.**

***Index Terms*—float, drifter, sensor platform, control system, state–space feedback, nonlinear control**

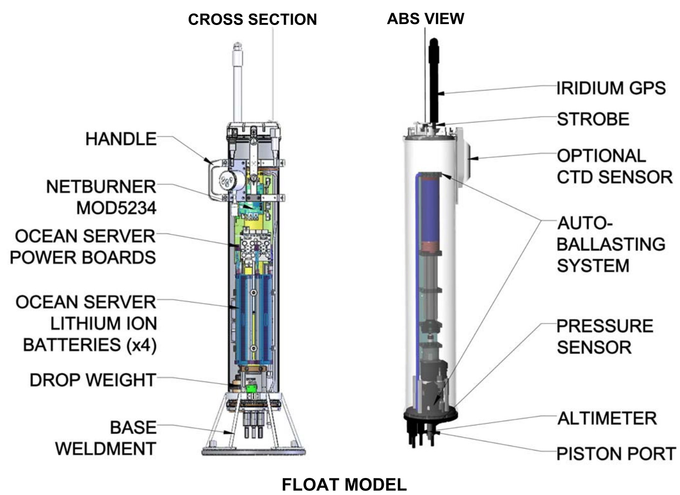

Fig. 1. The main components of the new mid–depth Lagrangian profiling float. The electronics consist of an Ocean Sever battery management system, four lithium ion 95 W–hr batteries, a NetBurner Mod 5234 microcontroller, and multiple feedback and scientific sensors. The Auto-Ballasting System consists of a motor driven piston mechanism and is driven by a controller that utilizes pressure and altitude readings. The optional CTD sensor can be attached depending on mission requirements. The top end cap contains housings for a GPS/Iridium antenna and a strobe. Additional housings are provided for other communications, such as radio and pre–mission networking.

I. Introduction

With the exponential growth in technology, the philosophy of a network of systems and sensors is driving advancements in ocean engineering systems every day. As part of this philosophy, Lagrangian floats play an important role with their ability to operate remotely and autonomously for long time scales over large areas [1]. Ideally, Lagrangian floats follow the three dimensional motion of a fluid parcel and track its motion over time. This concept allows for insights into ocean circulation which both compliments stationary instruments and provides observations not obtainable with static sensors alone.

While deep Lagrangian floats have a rich evolution in tracking global currents [2], there has been little emphasis on adapting the technology for shallow water coastal regions where the floats are subject to much lower pressures, but in many cases, more dynamic environments. These factors contribute to fundamental differences in these two classes of Lagrangian floats. While the deep Lagrangian floats must limit their buoyancy engines to lower speeds and higher mechanical advantages, mid–depth and coastal floats have much different restrictions. This enables their buoyancy engines and ultimately their performance to be improved drastically. These performance advancements are important because shallow waters can present a much more variable and turbulent environment. As an example, Eric D'Asaro, has deployed "Mixed Layer Lagrangian Floats (MLFII)" [3] with much larger volumes for buoyancy control. The speed and number of times these floats can profile is far greater than that of deep Lagrangian floats. Still, these floats are not well equipped for shallow water regions where the sea floor is within the float's operating range. Additionally, the control systems, which are comparable to those in deep Lagrangian floats, are often limited to basic trajectories with long rise times [1].

To satisfy this niche, the mid–depth profiling float has been designed to handle shallow water challenges, while advancing trajectory types, performance, and efficiency. Beyond these improvements, the float is designed to perform missions over several days and report back to the surface for retrieval. Be-

978-1-4244-5222-4/10/$26.00 ©2010 IEEE

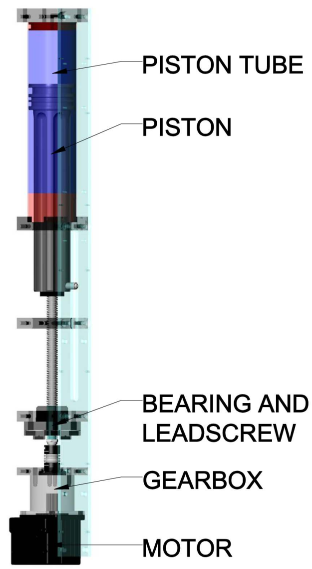

Fig. 2. Auto-Ballasting System (ABS). The ABS consists of a motor driven piston mechanism that either draws water into the piston tube, or flushes water out, changing the float's buoyancy.

cause this float is a modular design, the mission types can vary greatly. One mission could be primarily based on near–bottom work, while the float maintains a constant altitude. Another mission could consist primarily of rate controlled profiling with CTD readings between two user–defined depths. These new mid–depth Lagrangian profiling floats are designed to be a very versatile platforms that can support many oceanography studies.

II. Buoyancy Control

A. Auto-Ballasting System

To control buoyancy and therefore vertical movement, the float is equipped with an Auto–Ballasting System (ABS) that can drive water into or out of a piston tube within the float (Fig. 2). The volume of the piston tube with respect to the float is quite large so that the ABS can maintain performance in dynamic environments often associated with shallow waters. Essentially, by adjusting the volume of water within the piston tube, the effective volume of the float changes, thereby changing the buoyancy.

The total active volume (V_a) for buoyancy control is a function of the piston stroke (h) and plunger diameter (d_p) and area. This large volumetric change is required so that the float can handle dynamic environments and also so that the float can properly lift its iridium antenna high enough out of the water. This volume and its effect on the float dynamics is described in the following sections.

B. Animatics SmartMotor

The Animatics SmartMotors SM2315DT and SM2316DT-PLS2 (used in two new prototype Lagrangian floats) are

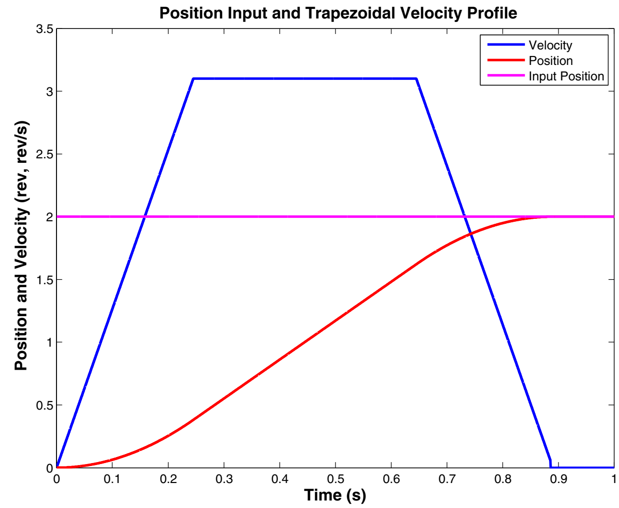

Fig. 3. SmartMotor position control. The SmartMotor SM2315DT and SM2316DT-PLS2 motors are DC brushless servo motors and contain an onboard PID controller to track position or velocity inputs. Both modes follow the trapezoidal constraints shown.

DC brushless servo motors that include microcontrollers with embedded PID control systems. [4] The PID controller and an integrated encoder are used to track position, velocity, or torque inputs. For position commands, the SmartMotor follows a trapezoidal velocity profile, meaning that it will accelerate at a specified constant until it reaches the maximum selected velocity. The velocity will then decelerate at the same rate until it again reaches zero such that when the motor stops moving, the position command will be reached. This yields a trapezoidal velocity profile which is standard for many servo motors. Fig. 3 shows this behavior.

Controlling the motor in velocity mode follows a similar procedure. In both modes, a maximum velocity and constant acceleration must be defined. These values are critical to the control system performance and efficiency and are discussed later in this paper. Fig. 3 also shows that the motor is inherently nonlinear in both control modes. In order to achieve linear control, the input signals must acknowledge the maximum position, velocity, and acceleration specifications. By driving the motor in position mode, while controlling the amplitude and period of a sinusoidal position input, linear control limits were established. However, when subject to a sinusoidal position command, the velocity showed much fluctuation due to the trapezoidal operation. Constantly accelerating the piston under load would contribute to additional power consumption. Velocity input tests produced much smoother acceleration profiles and simpler linear control restrictions. Although velocity control is not as intuitive, its advantages in terms of power consumption and linear control are significant. Therefore, the control system design utilizes velocity input control.

C. Float Dynamics

The system dynamics provide a foundation for specifying all system components in order to ensure the Lagrangian float's

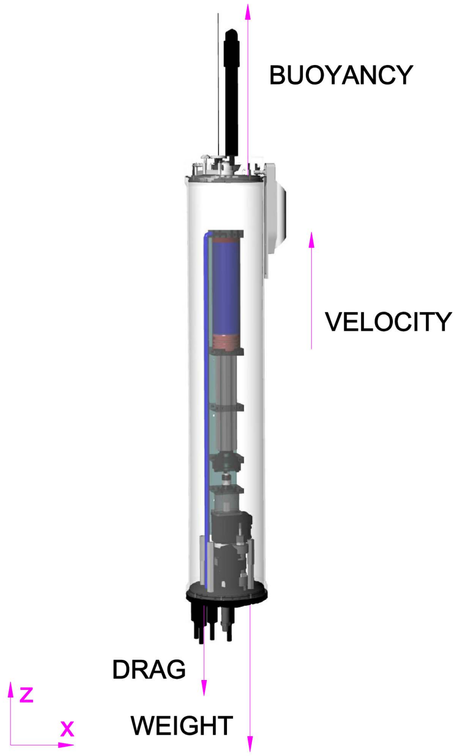

Fig. 4. The main forces acting on the moving float. The float is assumed to be ascending and therefore the buoyant force is greater than the weight of the float. As the float moves, it is also subject to a quadratic drag force. Additionally, an added mass term is considered, which accounts for the additional inertia provided by parcels of water working against the accelerating float.

physics are matched with the onboard Auto-Ballasting System (ABS). The main forces acting on the float include buoyancy, gravity, and drag as shown in Fig. 4. Added mass, which affects accelerating objects underwater, is also considered. This term is not actually derived, but is found empirically. The equation of motion considers these factors, and the influence of the ABS, which uses a piston to pull water into or out of the system, as illustrated in Fig. 2. By changing the volume of water contained within the float, the float's volume actually remains the same. Realistically, the float's mass is the only variable changing because the water pulled into the float must move with the float as well. Intuitively, it is more helpful to think of the ABS as a volume changing mechanism. It will be shown through the following derivation that this assumption is actually quite valid when the ABS volume is small compared to the float's volume. Additionally, this assumption is critical to a more simplified control system design. Note that in this derivation, the surface is the depth reference point, and depth is therefore negative. Also, note that the following equations use the variables and constants specified in Table I.

$$\sum F = F_b - F_d - F_w = (m + m_a)(z'') \tag{1}$$

TABLE I
FLOAT DYNAMICS CONSTANTS

Coefficient	Description	Units
z	float depth	m
z'	float velocity	m/s
z''	float acceleration	m/s^2
m_t	total float mass	kg
m_f	initial float mass	kg
m_a	added mass	kg
V_c	float's initial volume	m^3
V_p	volume of water in piston	m^3
A	float's cross sectional area	m^2
ρ_w	water density	kg/m^3
g	acceleration due to gravity	m/s^2
F_b	buoyancy force	N
F_d	drag force	N
F_w	weight	N

$$(m_t + m_a)(z'') = -\left(\frac{1}{2}AC_d\rho_w(z')^2\right) + (-m_t g) + (\rho_w g V_c) \tag{2}$$

Next, expand the total mass to be the sum of the float's initial mass, and the mass of the added water volume and substitute the result into (2).

$$m_t = m_f + \rho_w V_p \tag{3}$$

$$(z'') = \frac{-\left(\frac{1}{2}AC_d\rho_w(z')^2\right) - (m_f + \rho_w V_p)\, g + (\rho_w g V_c)}{(m_f + \rho_w V_p + m_a)} \tag{4}$$

Note that the final equation of motion correctly models the additional mass added to the system when the piston pulls water in. While this equation of motion is more accurate, one assumption can be made that significantly reduces the complexity of the system. The assumption is that the mass added to the system by a change in water volume in the ABS is sufficiently small compared to the total mass and added mass of the float. The reason this assumption is made is so that the input, or control variable V_p does not appear in the numerator and denominator of the system. While the equation of motion is still nonlinear after this simplification, shown in (5) it is much simpler with respect to nonlinear control methods.

$$(z'') = \frac{-\left(\frac{1}{2}AC_d\rho_w(z')^2\right) - m_f g + \rho_w g V_c - \rho_w g V_p}{(m_f + m_a)} \tag{5}$$

By comparing (5) and (2) for maximum acceleration, the error is found to be less than one percent and therefore this assumption is valid and will be used in the control system design.

III. Motor Performance

A. Motor Testing

This section covers the motor power consumption and efficiency. In these tests, pressure was simulated by an assembly consisting of a high capacity dive tank, compressor, pressure

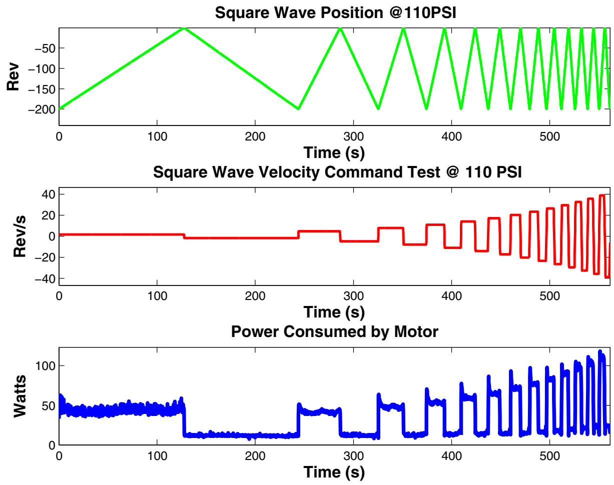

Fig. 5. Motor position, velocity, and power consumption for a square wave velocity input at 110 psi.

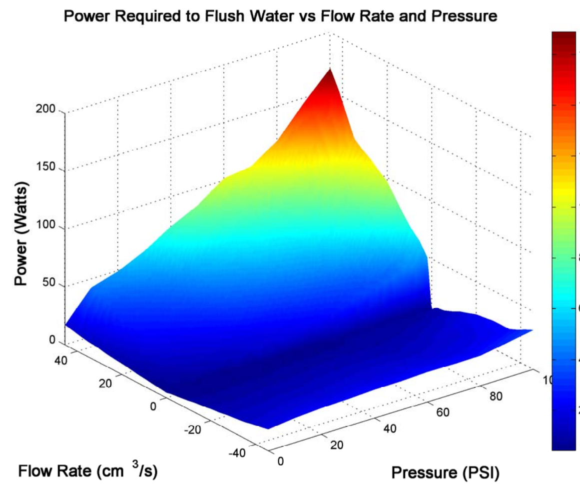

Fig. 6. SM2315DT power vs. flow rate and pressure.

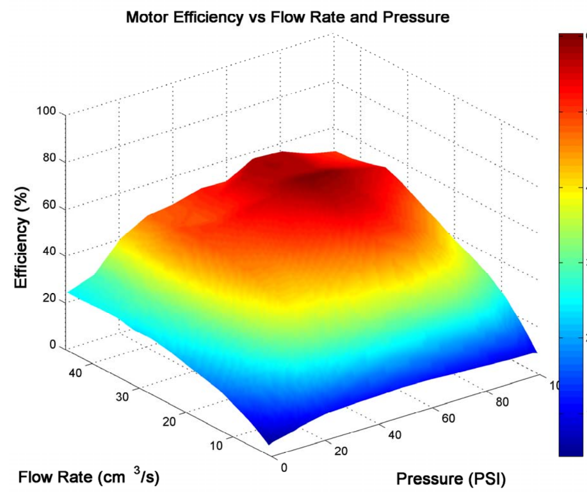

Fig. 7. SM2315DT efficiency vs. flow rate and pressure.

gauge, and valves. The motor was then commanded to go to a position at a certain maximum velocity and then stop and return to its original position. This simulates flushing out water to ascend, and then drawing water in to descend. The maximum motor velocity was increased through several iterations. This process was repeated from ambient pressure to the maximum stall pressure in steps of 10 psi. Both motor models were tested separately. For each test, the motor position, velocity, and power were found, as shown in Fig. 5.

It is evident that the power required to flush water against hydrostatic pressure is much greater than the power required to draw water into the system. Therefore, flushing power requirements is the main focus of the efficiency study.

B. Motor Power and Efficiency Models

By combining the motor testing results throughout all pressure and velocity ranges and averaging the values, accurate models for motor power and efficiency were developed. The SM2315DT power consumption is shown as a function of ABS flow rate and applied pressure in Fig. 6. A similar model was developed for the SM2316DT–PLS2 motor as well.

The efficiency is then found by comparing the power consumed with the theoretical mechanical power required to flush water at particular pressures and velocities. The mechanical power required to drive water at a given pressure with a constant velocity is a product of the constant torque the motor is subject to and the angular velocity at which it is driven. Referring back to the ABS in Fig. 2, L is the leadscrew lead, p is the applied pressure, A_p is the area of the piston, F_{fs} is the force of friction due to the seal, e_{ls} is the leadscrew efficiency, e_{gb} is the gearbox efficiency, N_r is the gearbox ratio, and the constant torque acting on the motor, τ_c is:

$$\tau_c = \frac{L\left(pA_p + F_{fs}\right)}{2\pi e_{ls} e_{gb} N_r} \tag{6}$$

The mechanical power (P_m) required from the motor is then a product of the constant torque and the motor's angular velocity (ω):

$$P_m = \tau_c \omega \tag{7}$$

Next, the power results in Fig. 6 are divided by the theoretical values found in (7).

The efficiency peaks at relatively high flow rates and pressures. However, at low flow rates, meaning slow motor velocities, the efficiency of the motor decreases significantly. It therefore appears that limiting the speed of the ABS to low values will not efficiently utilize the available energy. However, the tradeoffs between speed, float performance, and energy requirements aren't as intuitive and require simulations to optimize the tradeoffs. These are described in later sections.

IV. Control System Design

A. Control System Goals

The control system design must provide a robust, adaptable, and tunable system to handle several input trajectory types, including step, profiling, and bottom tracking behaviors, which

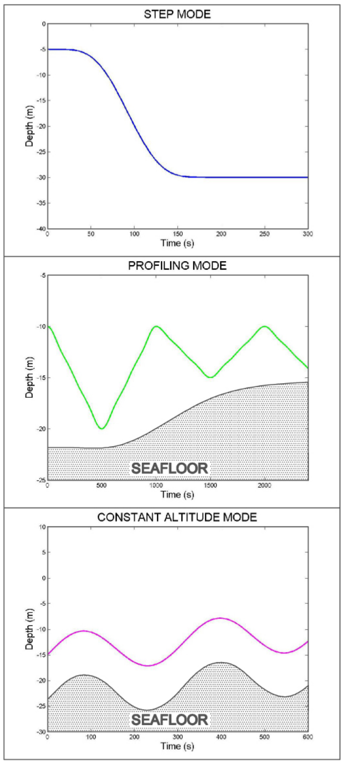

Fig. 8. Main float trajectory behaviors. These include step inputs to constant depths, profiling inputs with adjustable rates and adaptable limits, and a constant altitude mode.

are shown in Fig. 8 and discussed in detail throughout this section.

Each of these control modes must be optimized for performance and efficiency by combing simulations with real motor power consumption data obtained from testing. While these modes are optimized, adaptability must be considered as well. For instance, if the float is rigged with an extra instrumentation package that changes its mass, drag, buoyancy, or the float's dynamics by any means, the control system must make respective adjustments. A related calibration routine must also be implemented. These goals will be considered throughout all three modes of operation.

B. PID Controller Shortcomings

Last generation's float [5] utilized a Proportional–Integral–Derivate (PID) controller which was effective but difficult to optimize. PID controllers are quite common because they use a generic equation that can be customized to specific systems by toggling gain values. The PID uses a weighted sum of errors containing the proportional term which indicates the current error value, integral term which considers the buildup of errors, and derivative term which considers the rate of change in the error. The problem with this method is that the best way to optimize the weight that each term is scaled by is to either guess and check, or run a time expensive cost function that simulates all combinations of the PID weights. If the system changes at all, then the optimal values must be

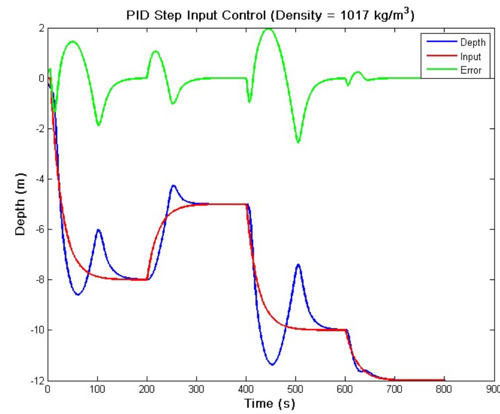

Fig. 9. PID shortcomings. The results of a controller tuned for performance in water with a density of 1025 kg/m^3.

found all over again. This doesn't offer much support for a system that is supposed to be modular and appear in different configurations. In some cases acceptable results were obtained after fine tuning the gain parameters. However, as soon as even one condition was tweaked, the performance degraded quickly. For instance, Fig. 9 shows the results of a PID simulation in which the water density was changed from 1025 kg/m^3 to 1017 kg/m^3. This small change produces undesirable results unless the PID controller is tuned again. Because of the several shortcomings presented here, the next section describes the development of a state–space control system.

C. State–Space Control with Linearizing Feedback

Despite the nonlinear equation of motion describing the float's movement, state–space control with linear techniques can be employed after a change of variables known as feedback linearization. While state–space control requires an accurate model of the system and feedback from a minimum set of states that fully describes the system, high performance results and adaptability can be achieved.

First, (5) is reduced to the following:

$$z'' = \alpha_1 \left((z')^2 \right) sgn\left(z'\right) + \alpha_2 + \alpha_3 V_p \tag{8}$$

Where $\alpha_1 = \frac{-\frac{1}{2} A C_d \rho_w \left(z'\right)^2}{m_f + m_a}$, $\alpha_2 = \frac{-mg + \rho_w g V_c}{m_f + m_a}$, and $\alpha_3 = \frac{-\rho_w g}{m_f + m_a}$. The state vector is then:

$$\underline{x}(t) = \begin{bmatrix} x_1(t)) \\ x_2(t)) \\ x_3(t)) \end{bmatrix} = \begin{bmatrix} z \\ z' \\ V_p \end{bmatrix} \tag{9}$$

Where $z =$ float position, $z' =$ float velocity, and $V_p =$ piston volume. Also note that $u = V_p' =$ piston volume rate.

The input is chosen to be the piston volume rate, which is directly related to motor testing results that showed excessive velocity ramping in position control mode, leading to additional power consumption. The resulting state–space description is:

$$\underline{x}' = \underline{f}\left(x, u\right)$$

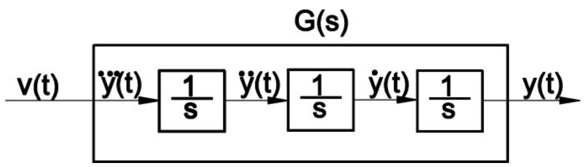

Fig. 10. Triple integrator plant.

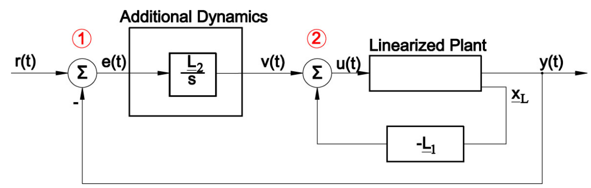

Fig. 12. Design Model.

$$x_1' = x_2$$
$$x_2' = \alpha_1 (x_2)^2 \, sgn\,(x_2) + \alpha_2 + \alpha_3 x_3$$
$$x_3' = u$$

Or,

$$\underline{x}'(t) = \begin{bmatrix} x_1'(t) \\ x_2'(t) \\ x_3'(t) \end{bmatrix} = \begin{bmatrix} z' \\ z'' \\ V_p' \end{bmatrix} = \begin{bmatrix} x_2 \\ \alpha_1 (x_2)^2 \, sgn\,(x_2) + \alpha_2 + \alpha_3 x_3 \\ u \end{bmatrix} \tag{10}$$

Equation (10) shows that the state–space description is nonlinear, and therefore can't be controlled with linear methods without a transformation. Feedback linearization can be applied to several systems of this form. This method requires differentiating the output, y, of the system n times until the input variable appears. [6] Next, a virtual input variable, v, is set equal to the nth derivative of the output. The equation is then solved for the original input variable, u, such that this input will contain linearizing feedback terms. The plant state vector then consists of the $n+1$ state variables obtained through this method.

$$y = x_1$$
$$y' = x_1' = x_2$$
$$y'' = x_2' = \alpha_1 (x_2)^2 \, sgn\,(x_2) + \alpha_2 + \alpha_3 x_3$$
$$y''' = 2\alpha_1 x_2 x_2' sgn\,(x_2) + \alpha_3 x_3'$$
$$y''' = 2\alpha_1 x_2 \left[\alpha_1 (x_2)^2 \, sgn\,(x_2) + \alpha_2 + \alpha_3 x_3\right] sgn\,(x_2) + \alpha_3 u$$

On the third derivative of the output, the input variable appears. Next, the terms are rearranged:

$$y''' = 2\alpha_1^2 x_2^3 + 2\alpha_1\alpha_2 sgn\,(x_2) + 2\alpha_1\alpha_3 x_2 x_3 sgn\,(x_2) + \alpha_3 u \tag{11}$$

Finally, the third derivative of the output is set to the virtual input variable v, and the resulting equation is solved for u which now contains linearizing feedback:

$$y''' = v = 2\alpha_1 x_2 \left[\alpha_1 (x_2)^2 \, sgn\,(x_2) + \alpha_2 + \alpha_3 x_3\right] sgn\,(x_2) + \alpha_3 u$$

$$u = \frac{-1}{\alpha_3}\left[2\alpha_1 x_2 sgn\,(x_2)\left(\alpha_1 x_2^2 sgn\,(x_2) + \alpha_2 + \alpha_3 x_3\right) - v\right] \tag{12}$$

The linearized plant can then be thought of as a triple integrator with the state vector $\underline{x}_L(t)$ (in terms of the original state variables) equal to a vector consisting of $y(t)$ and its n derivatives or:

$$\underline{\mathbf{x}}_L(t) = \begin{bmatrix} y(t) \\ y'(t) \\ y''(t) \end{bmatrix} = \begin{bmatrix} x_1(t) \\ x_2(t) \\ \alpha_1 (x_2)^2 \, sgn\,(x_2) + \alpha_2 + \alpha_3 x_3 \end{bmatrix} \tag{13}$$

With a state space equation as follows:

$$\underline{\mathbf{x}}_L'(t) = \mathbf{A}\underline{\mathbf{x}}_L(t) + \underline{\mathbf{b}}v(t)) \tag{14}$$
$$y(t) = \underline{\mathbf{c}}\,\underline{\mathbf{x}}_L(t) \tag{15}$$

$$\mathbf{A} = \begin{bmatrix} 0 & 1 & 0 \\ 0 & 0 & 1 \\ 0 & 0 & 0 \end{bmatrix}, \ \underline{\mathbf{b}} = \begin{bmatrix} 0 \\ 0 \\ 1 \end{bmatrix}, \ \underline{\mathbf{c}} = \begin{bmatrix} 1 & 0 & 1 \end{bmatrix} \tag{16}$$

The linearized plant model then appears as shown in Fig. 11. State variables of the float model, $x_1(t)$ (float depth), and $x_3(t)$ (piston volume) can be measured directly while the float velocity must be found differentially or through the use of an observer. For now, a differentiator is assumed.

D. Step Inputs

Now that a linearized plant has been developed and modeled as a triple integrator, a state–space control system can be designed to track step inputs, profiling inputs, and constant altitude inputs. The basic design for such a system is shown in Fig. 12. The design model consists of the linearized plant, an additional dynamics block, and a feedback vector for pole placement. Fig. 12 shows one realization of the additional dynamics block. In this case, it is shown to be an integrator which is typically chosen for step input tracking. This architecture requires that the poles of the input be included in the eigenvalues of the additional dynamics for tracking [7].

Next, the feedback vector is calculated using the well known feedback gain formula [7] and normalized Bessel polynomials to achieve the desired settling time. While the settling time can be continually adjusted, and therefore require different feedback gains for different size step inputs, utilizing shaped inputs is more effective. A shaped input can remove the discontinuities associated with a step input and smooth the transition over the amplitude. Additionally, shaped inputs can be designed to match realistic hardware limitations. Traditionally, a sinusoidal acceleration profile is used. A sinusoidal acceleration ensures the system is at rest to begin and end the trajectory. It also provides a smooth transition to the maximum velocity halfway through the trajectory, at which point it begins to decelerate. Through a double integration, the position input signal is found.

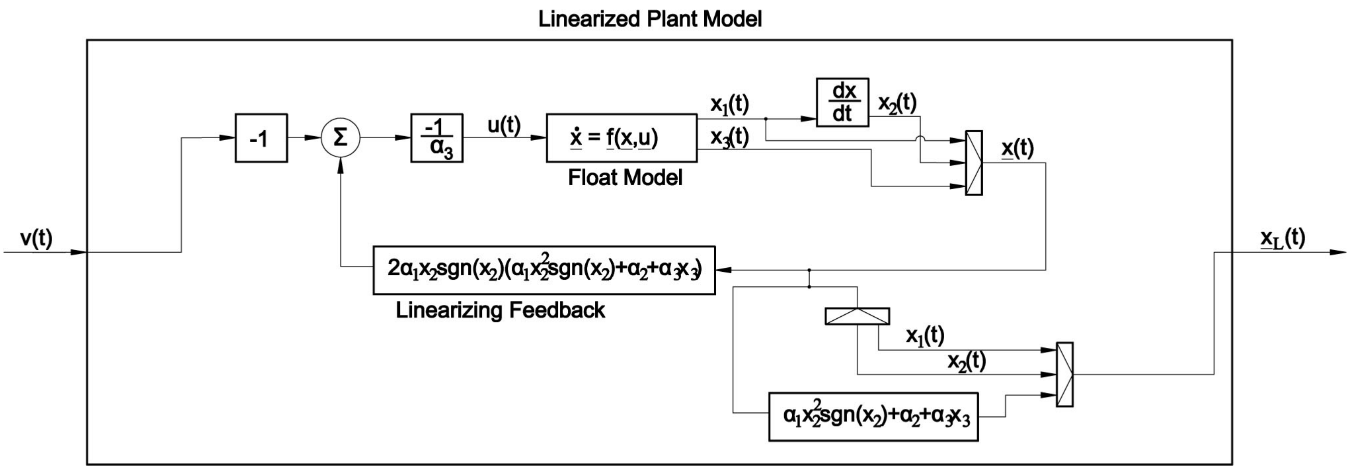

Fig. 11. Linearized Plant Model.

E. Profiling with Triangle Wave Inputs

In order to design a tracking system for a triangle wave, the additional dynamics must be designed so that poles of the reference input are included in the eigenvalues of the additional dynamics. Because there is no rational input for a triangle wave [7], the Fourier series expansion is calculated and shown in (17):

$$r(t) = \sum_{\substack{n=1 \\ odd}}^{\infty} \left[\frac{8A}{\pi^2 n^2} sin\left(n\omega_o t\right) \right] \tag{17}$$

Where A is the amplitude, and ω_o is the fundamental frequency. The number of terms used from the expansion will affect the accuracy of the triangle wave representation, and the complexity of the additional dynamics. To obtain a highly accurate triangle wave, several Fourier series terms must be included. However, it is found that two or three terms are sufficient, as shown in the Fig. 14. The approximated triangle wave obtained from the Fourier series expansion can be scaled to any amplitude of interest for the profiling mode once the additional dynamics block is designed to match the poles of the input. However, from (17), it is apparent that the Fourier series, and therefore the additional dynamics pole locations are unique to the profiling frequency. This limits

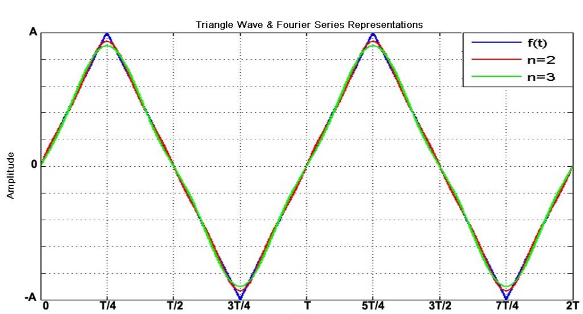

Fig. 13. Fourier series representation of a triangle wave for profiling modes.

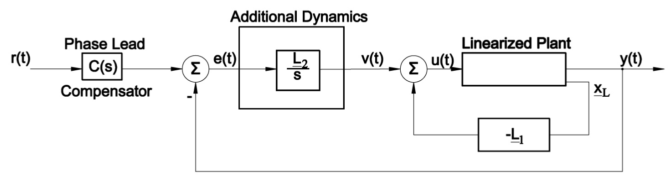

Fig. 14. Design Model with phase lead compensator.

the adaptability of the profiling mode, and complicates the initialization. However, a solution is presented in the next section with the development of a constant altitude controller with a phase lead compensator.

F. Constant Altitude with Phase Lead Compensator

In order to ensure that the constant altitude mode would react quickly to disturbances, a phase lead compensator was implemented. The phase lead ensures that the system responds quickly to changes in bottom topography by compensating for the inherent system lag. The compensator is a high pass design that will compensate for the inherent high frequency roll off of the design model and enable the system to respond rapidly to changes in bottom topography, only limited by the float's physical response time and sensor sampling rate. Typically the compensator is the inversion of the design model transfer function. This allows the poles of the compensator to cancel out the zeros of the design model, and faster pole locations to be placed in the compensator. The compensator gain is also calculated to be zero at DC. The control system with a phase lead compensator is shown in Fig. 14.

Traditionally, a separate controller with additional dynamics to match the input trajectory is need for each trajectory type. However, the development of the bottom tracking controller lead to a system with a frequency response that is sufficient for several trajectory modes. After the system simulations demonstrated successful responses to various bathymetry, the phase lead compensated control system was issued triangular wave inputs and produced comparable results to the system designed specifically for triangular waves. For this reason, this controller was chosen as a standalone controller to handle all input types. Initially, several controllers were needed and this complicated the overall control system.

G. *Full State Observer and Noise*

One of the issues with state–space control systems is that the control system needs to know the state of all variables in the state vector. This is often difficult as some properties cannot be easily measured. In this case, the velocity of the float is not measured. One way to compensate for this is to differentiate the position. Unfortunately, this simplistic approach is very vulnerable to noise. Simulations show that the float may even begin to oscillate if velocity is obtained through differentiation. To provide a better estimate of the float's velocity, a full state observer can be used. The observer essentially uses the float model and the input and output values to drive the error in its estimates to zero [7]. Fig. 15 shows the entire control system in digitized form with the integrated observer.

V. Control System Simulation

A. *Step Inputs*

The control system shown in Fig. 15 is simulated in Simulink and combined with Matlab scripts to estimate power and energy consumption from the motor power models. Fig. 16 shows a typical step input response and the associated power consumption derived from the motor models. After several simulations and consideration of results from lab testing, the maximum allowable ABS flow rate was chosen to be 23.6 cm^3/s. In many cases, the settling time showed diminishing returns for higher flow rates. Additionally, higher flow rates at high pressure can lead to motor stalling and over–current faults. The reason the resulting flow rates displayed for this trajectory do not approach the prescribed maximum is that the maximum float acceleration rate chosen for the shaped input considers all step amplitude sizes. This value is chosen to ensure the float is not issued an impossible trajectory to follow, which would likely result in overshoot. These results indicate that for large amplitude step inputs, sinusoidal shaped inputs are rather sluggish.

Notice the settling time, T_s is 179 s and the energy required by each motor is roughly 2500 J for a 30 m sinusoidal shaped step response. While results for small amplitude sinusoidal shaped step responses are more favorable, an alternate method for large amplitude step responses was developed. Based on the understanding that the motor consumes far less power while stationary, due to the locking characteristic of the ACME leadscrew, a cubic shaped input, with a maximum velocity placed just above the float's attainable velocity was designed. A properly designed cubic input can exhibit a nearly constant slope over much of its transition around its point of inflection. By starting with the derivative of the cubic, and specifying the maximum velocity and then the start and stop positions, a properly shaped cubic can be obtained. The benefits for large amplitude inputs are significant. Fig. 17 shows the results

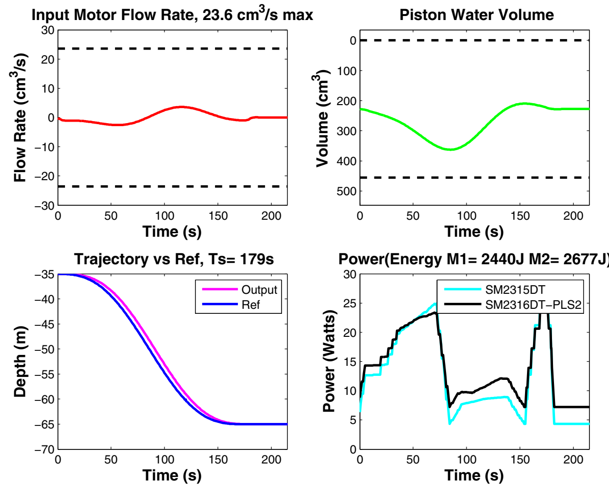

Fig. 16. Step input response for a sinusoidal shaped input.

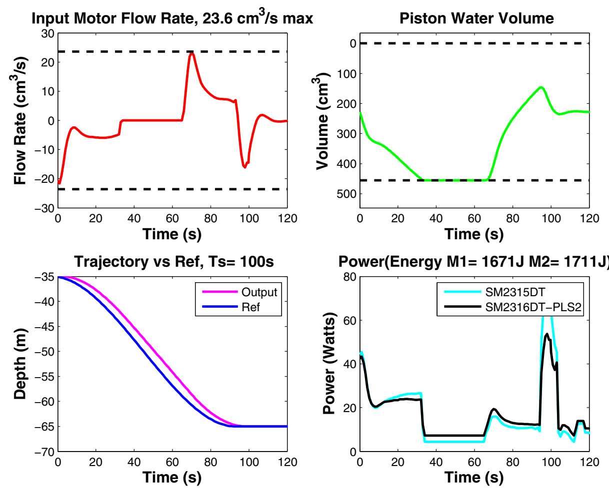

Fig. 17. Step input response for a cubic shaped input.

for the same amplitude step input in Fig. 16. Note that the settling time is cut down from 179 s to 100 s, while the energy required is also significantly reduced. These results have prompted more research in shaped inputs. Ideally, the shaped input will be perfectly matched to the float's dynamics.

B. *Profiling and Constant Altitude*

The significance of a standalone controller with fixed pole locations and a phase lead compensator is pronounced when used for profiling control. As long as the frequency and amplitude of the input triangular wave are physically attainable by the float, then the control system tracks with minimal error. In a specifically designed state–space tracking system, the additional dynamics pole locations would have to match those of the reference input. This complicates the overhead for control system calculations and limits the adaptability. With the standalone controller, profiling rates, periods, and amplitudes can be adjusted on the fly to reflect mission criteria and bathymetry. Consider a ledge that interferes with the

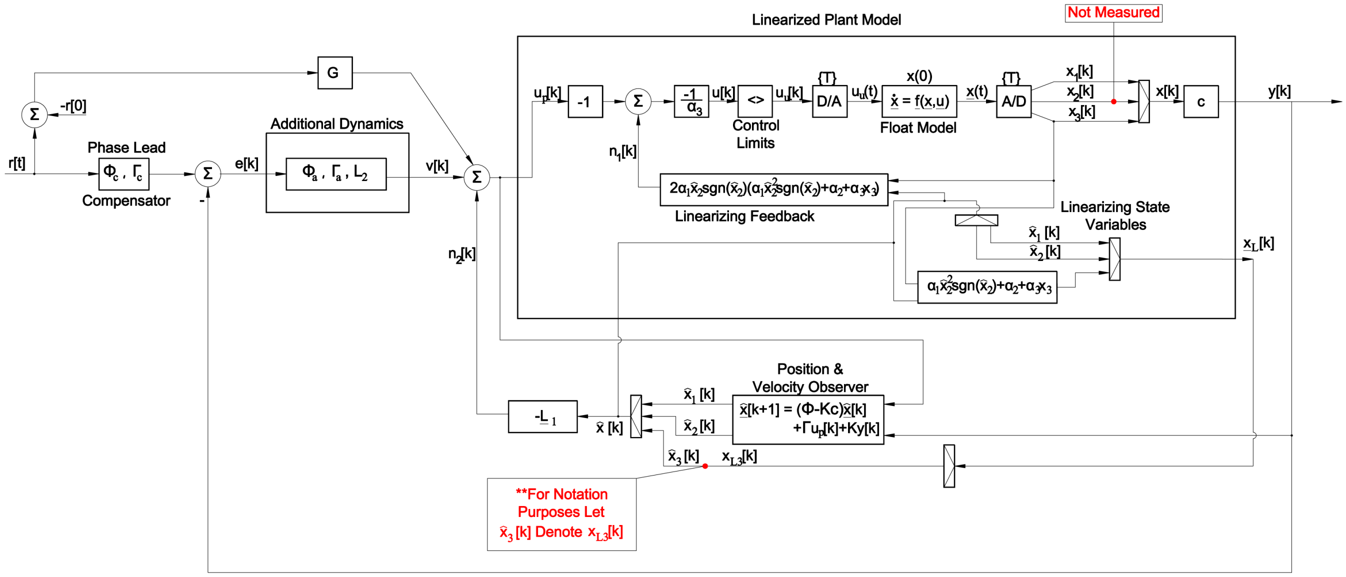

Fig. 15. Control system block diagram. This system handles step inputs, profiling inputs with adjustable rates and adaptable limits, and constant altitude bottom tracking.

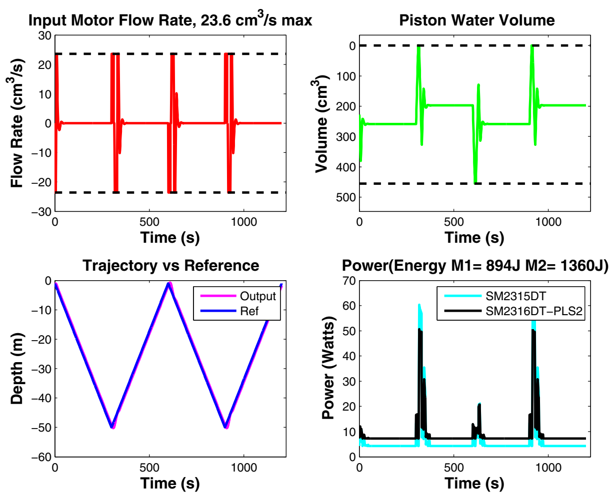

Fig. 18. Profiling mode.

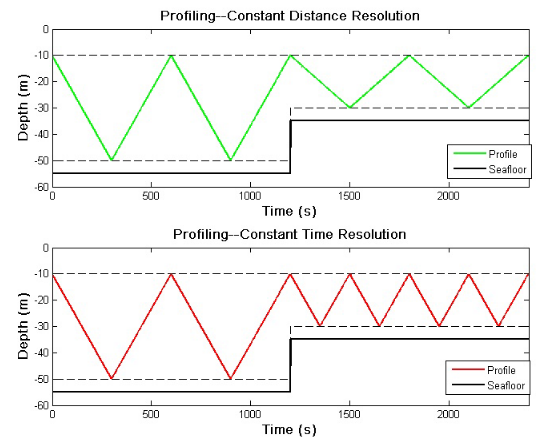

Fig. 19. The profiling float encounters a ledge at 1200 seconds and immediately adjusts its amplitude and vertical offset to ensure the float maintains a minimum 5 meter offset from the sea floor. In constant distance resolution mode, the profiling period doesn't change with respect to time and conserves constant horizontal sampling (assuming a constant drift rate). In constant time resolution mode, the profiling period is adjusted to conserve a constant profiling rate with respect to time. Therefore the slopes of each profile with respect to time are identical. The horizontal distance between each profile is not conserved.

float's profiling trajectory. In order to avoid contact with the bottom, the amplitude must be changed. If only the amplitude and vertical offset are modified, then the profiling velocity is changed. While this may be desirable for constant horizontal resolution, CTD profiles commonly preserve the profiling velocity. This requires a change in the profiling frequency. With the phase lead compensated state–space feedback control system both methods shown in Fig. 19 are possible.

The concepts described for the profiling mode are directly applicable to the constant altitude mode. In fact, the profiling mode includes a minimum altitude shown in Fig. 19. Constant altitude operation is actually a simplified version of the adaptive profiling mode described. In constant altitude mode, the depth reading from the pressure sensor will serve as the main input, while the altitude is averaged over several seconds to determine an appropriate small amplitude step input. This technique is used because the float will be drifting rather slowly and the altitude reading from the acoustic altimeter is subject to more noise than the pressure sensor.

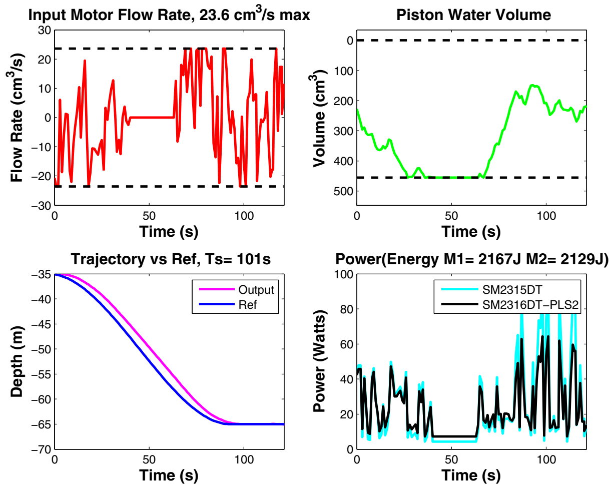

Fig. 20. Step input response for a sinusoidal shaped input with up to 4 cm of white noise.

C. Noise

With low noise levels in pressure readings, the control simulations shown throughout this section are quite accurate. However, if substantial noise is introduced into the system, the full state observer will ensure that the sensor feedback readings are usable. Simulations with pressure readings subject to white noise up to 4 cm show that the float remains controllable, but consumes additional power due to a noisy input velocity signal. Simulations with noise applied to the trajectory shown in Fig. 16 and Fig. 17, for a cubic shape step input are still acceptable. Fig. 20 shows such results.

VI. Conclusions and Outlook

This paper has covered the design of a new mid–depth Lagrangian profiling float with a high efficiency state–space control system with linearizing feedback. The control system uses pressure and altitude readings to perform advanced adaptable trajectories for different sensor platforms. The main operating modes of this float include step inputs, adaptable profiling inputs, and constant altitude bottom tracking. This Lagrangian float design is unique with its advanced performance abilities in shallow water regions and therefore lends itself to a variety of oceanography studies. The control system design covered in this paper will be implemented and tested in a new float that is currently under construction. In addition, the control system will be upgraded to include a calibration routine in order to increase the accuracy of the float dynamics model in the control system. This will ensure that the float can adapt to a variety of conditions and handle different equipment packages while maintaining peak performance, rendering it a very versatile sensor platform for future deployments.

VII. Acknowledgments

The authors would like to thank Dr. Robert J. Vacarro for his help in the control system design, Todd Gregory for his help with the mechanical design, and Henry Sharpe III. for his help in systems engineering, and electronic and software design. For more information please contact the authors or Bluewater Designworks, LLC (sales@BluewaterDesignworks.com).

References

[1] D. Roemmich, S. Riser, R. Davis, and Y. Desaubies, "Autonomous profiling floats: Workhorse for broad-scale ocean observations," *Marine Technology Society Journal*, vol. 38, no. 1, pp. 31–39, 2004.
[2] T. Rossby, E. R. Levine, and D. N. Conners, "The isopycnal Swallow float: A simple device for tracking water parcels in the ocean," vol. 14, pp. 511–525, 1985.
[3] E. A. D'Asaro, "Performance of autonomous lagrangian floats," *Journal of Atmospheric and Oceanic Technology*, vol. 20, pp. 896–911, 2003.
[4] "The smart motor series 4 user guide rev. 5," Animatics.
[5] A. Schwithal and C. Roman, "Development of a new lagrangian float for studying coastal marine ecosystems."
[6] J. K. Hedrick and A. Girard, *Control of Nonlinear Dynamic Systems: Theory and Applications*, 2005.
[7] R. J. Vacarro, *Digital Control: A State-Space Approach*. McGraw Hill, USA, 1995.
[8] J. Swallow, "A neutral-buoyancy float for measuring deep currents," vol. 3, pp. 74–81, 1955.
[9] J. C. Swallow and L. V. Worthington, "An observation of a deep countercurrent in the western North Atlantic," vol. 8, pp. 1–19, 1961.
[10] T. Rossby, J. Price, and D. Webb, "The spatial and temporal evolution of a cluster of SOFAR floats in the POLYMODE Local Dynamics Experiment (LDE)," *Journal of Physical Oceanography*, vol. 16, pp. 428–442, 1986.
[11] H. T. Rossby, A. D. Voorhis, and D. Webb, "A quasi-Lagrangian study of mid ocean variability using long-range SOFAR floats," vol. 33, pp. 355–382, 1975.
[12] M. D. Prater and T. Rossby, "Observations of the Faroe Bank Channel overflow using bottom-following RAFOS floats," vol. 52, pp. 481–494, 2005.
[13] J. Jaffe, R. Glatts, C. Schurgers, D. Mirza, P. Franks, P. Roberts, and F. Simonet, "Aue: An autonomous float for monitoring the upper water column," in *OCEANS 2007 - Europe*, 2007.
[14] G. L. Hitchcock, E. J. Lessard, D. Dorson, J. Fontaine, and T. Rossby, "The IFF: The isopycnal float fluorometer," vol. 6, pp. 19–25, 1989.
[15] R. E. Davis, D. C. Webb, L. A. Regier, and J. Dufour, "The Autonomous Lagrangian Circulation Explorer (ALACE)," vol. 9, pp. 264–285, 1992.
[16] A. S. Bower, B. L. Cann, T. Rossby, W. Zenk, J. Gould, K. Speer, P. L. Richardson, M. D. Prater, and H.-M. Zhang, "Directly measured mid-depth circulation in the northeastern North Atlantic Ocean," vol. 419, pp. 603–607, 2002.
[17] H. J. Freeland, P. B. Rhines, and T. Rossby, "Statistical observations of the trajectories of neutrally buoyant floats in the North Atlantic," vol. 33, pp. 383–404, 1975.
[18] http://www.ocean-server.com/converters.html, Ocean Server Technology.
[19] http://www.netburner.com, NetBurner.